Acta Cryst B STRUCTURAL SCIENCE CRYSTAL ENGINEERING MATERIALS

ISSN 2052-5206

Correlated disorder and crystal structure of β-$VOSO_4$

Chloe A. Fuller,[a]* Diana Lucia Quintero-Castro,[b] Alexei Bosak,[c] Vadim Dyadkin[a] and Dmitry Chernyshov[a]

[a]SNBL at ESRF, Grenoble, France, [b]Department of Mathematics and Physics, Universitetet i Stavanger, 4036 Stavanger, Norway, and [c]ESRF, Grenoble, France. *Correspondence e-mail: chloe.fuller@esrf.fr

Received 22 June 2022
Accepted 17 October 2022

Edited by M. de Boissieu, SIMaP, France

Keywords: diffuse scattering; single-crystal diffraction; structural disorder; Monte carlo modeling.

CCDC reference: 2213556

Supporting information: this article has supporting information at journals.iucr.org/b

Pauflerite β-$VOSO_4$ has recently been identified as a one-dimensional $S = \frac{1}{2}$ Heisenberg system, of interest both from a fundamental point of view and a potential material for future spintronics applications. The observation of diffuse scattering in a synthetic β-$VOSO_4$ provides a microscopic interpretation of the underlying correlated disorder, which is linked to the inversion of the short–long V—O distance pairs along VO_6 chains, forming a local defect state. Direct Monte Carlo modeling indicates that such defects form thin layers with a positive inter-layer correlation, forming small domains with inverted vanadyl bonding patterns. Two-dimensional defects in anisotropic magnetic systems may perturb, or even destroy, long-range magnetic ordering leading to unusual interactions. In particular, the lack of inversion symmetry in the defect layers opens up the possibility for the Dzyaloshinskii–Moriya interaction (DMI) and, consequently, chiral magnetism localized in the defect planes. The defect β-$VOSO_4$ structure, therefore, opens up new possibilities for the study of low-dimensional magnetic systems.

1. Introduction

Disorder in bulk materials, particularly those with low-dimensional structural building blocks, is an important ingredient of the physics underpinning their unique and technologically relevant properties. Prominent examples of this include superconductivity in systems of weakly bound 1D chains which can be enhanced by disorder (Petrovic *et al.*, 2016), the appearance of spin-Peierls instabilities in $S = \frac{1}{2}$ finite spin chains (Seidel *et al.*, 2003), the creation of edge states in $S = \frac{3}{2}$, two spin chains, and broken hidden symmetries in $S = 1$ spin chains (Qin *et al.*, 1995; Fang *et al.*, 2021), as well as strong effects in the transport and magnetic properties of 1D and 2D systems (Chávez *et al.*, 2021; Xiao *et al.*, 2020). These low-dimensional magnetic systems are of interest both from the fundamental point of view (Vasiliev *et al.*, 2018; Haldane, 1983), and as prospective materials for future quantum information technologies (Marchukov *et al.*, 2016; Mathew *et al.*, 2020; Laurell *et al.*, 2021), for which understanding structure–property relationships is a key component of development.

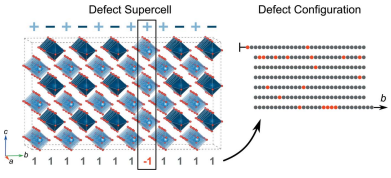

Various V^{4+}-containing materials are known to exhibit such low-dimensional magnetic interactions (O'Connor *et al.*, 1994), and the compound β-$VOSO_4$, with natural analog pauflerite (Krivovichev *et al.*, 2007), presents a particularly interesting case. Having been previously described as showing long-range antiferromagnetic ordering by Longo & Arnott (1970) and ferrimagnetic behavior by Villeneuve *et al.* (1989), β-$VOSO_4$ has been recently identified as a textbook $S = \frac{1}{2}$

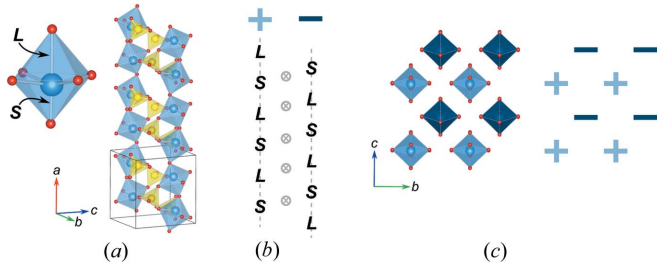

Figure 1
The crystal structure of β-$VOSO_4$. (*a*) A single distorted VO_6 octahedron with short (vanadyl, S) and long (L) bonds. The octahedra are connected in chains, propagating along the *a*-axis with alternating bonding patterns. (*b*) Schematics of the bonding patterns for the two neighboring chains, gray crossed dots indicate inversion centers. (*c*) The VO_6 substructure, viewed down the *a*-axis, showing the alternating vanadyl bonding pattern.

Heisenberg antiferromagnet (Quintero-Castro *et al.*, 2022, in preparation).

The crystal structure is built from distorted VO_6 octahedra with one short (vanadyl bond, 1.607 Å), four intermediate (1.992–1.996 Å), and one long (2.267 Å) V—O bond distances. The corner-sharing octahedra form folded chains propagating along the *a*-direction, with a strict alternating short-long bonding pattern. SO_4 tetrahedra link neighboring chains which have opposite bonding patterns, in agreement with the inversion symmetry (Fig. 1). Magnetic interactions are present both within the VO_6 chains, and between neighboring chains, mediated by V–SO_4–V superexchange. The latter interactions are very sensitive to geometrical distortions, in particular to small variations of the V—O—S bond angles, and vary from ferromagnetic for α-$VOSO_4$ to antiferromagnetic for $VOSO_4$·H_20 (Villeneuve *et al.*, 1989). These structural distortions and associated changes in magnetic interactions can be easily affected by structural disorder, that, when present, may become an important ingredient of the low-dimensional magnetism.

Here we report on the observation of the diffuse scattering in a synthetic β-$VOSO_4$, and provide a microscopic interpretation of the underlying correlated disorder. The very nature of the disorder is linked to the inversion of the short-long V—O distance pairs along the chains, forming a local defect state. Diffuse scattering indicates that such defects form thin layers, destroying the alternation of the V—O bonding pattern in the neighboring chains. We present an atomistic realization of the disordered crystal structure derived from Monte Carlo (MC) modeling, and discuss the possible interplay between disorder and magnetic properties.

2. Experiment

Single crystal samples of β-$VOSO_4$ were synthesized through the reaction $V_2O_5 + 2H_2SO_4 \rightarrow 2\beta$-$VOSO_4 + 2H_2O + 0.5O_2$, following Sieverts & Mueller (1928) as described by Quintero-Castro *et al.* (2022, in preparation). The resultant single crystals have a dark green color and needle-like shape (extending to a couple of mm), growing along the crystallographic *a*-direction.

Table 1
Crystal data and structure refinement at 293 K.

Empirical formula	$VOSO_4$
Formula weight	163.00
Wavelength (Å)	0.69027
Crystal system, space group	Orthorhombic, *Pnma*
Unit-cell dimensions (Å)	a = 7.39080 (10)
	b = 6.28640 (10)
	c = 7.09810 (10)
Volume (Å^3)	329.789 (8)
Z	4
Calculated density (Mg m^{-3})	3.283
Absorption coefficient (mm^{-1})	3.209
F(000)	316
Crystal size (mm)	0.02 × 0.02 × 0.05
Theta range (°) for data collection	3.866–32.873
No. of reflections collected, unique, R_{int}	2593, 664, 0.0306
Completeness to θ = 24.467°	98.8
Refinement method	Full-matrix least-squares on F^2
No. of data, restraints, parameters	664, 0, 44
Goodness-of-fit on F^2	1.177
Final R indices [$I > 2\sigma(I)$]	R_1 = 0.0264, wR_2 = 0.0702
R indices (all data)	R_1 = 0.0268, wR_2 = 0.0706
Largest difference peak and hole (e Å^{-3})	0.846 and −0.86

Single crystal Bragg and diffuse scattering data were collected at the BM01 end station of the Swiss–Norwegian Beamlines at the ESRF (Grenoble, France), on the Pilatus@SNBL diffractometer (Dyadkin *et al.*, 2016). For the Bragg data, the wavelength was set to λ = 0.69027 Å (17.96 keV), the detector was in its closest position (0.139 m) and the exposure time was 2 s per 1° of rotation. For the diffuse scattering, the wavelength was 0.68949 Å the sample–detector distance was 0.639 m, and data were collected for 10 s every 0.1°. Additional datasets were measured at the ESRF ID28 side station (Girard *et al.*, 2019) with a wavelength of 0.980 Å and 0.5 s per 0.25° sampling. Each dataset used a single axis full rotation around ω.

The Bragg data were processed with *CrysAlis Pro* software (Rigaku Oxford Diffraction, 2015) and the structure solved with *SHELXT*, then refined with *SHELXL* (Sheldrick, 2008). Representative parameters characterizing the Bragg data and structural refinement are given in Table 1.

3. Results and discussion

The refined average structure agrees well with previous structural reports, with one minor but significant addition:

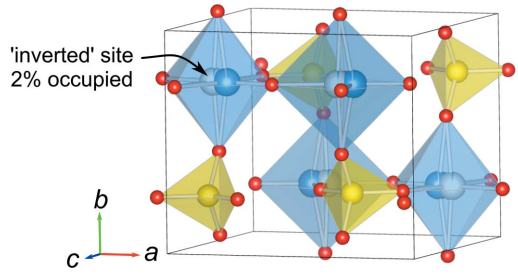

Figure 2
The refined average structure of $VOSO_4$, with blue and yellow polyhedra representing VO_6 and SO_4 units, respectively.

some low residual density positioned 0.6 Å away from vanadium and opposite to the vanadyl bond (Fig. 2). Inspection of reciprocal space shows no indications of non-/partial-merohedral twinning, and the refined average structure has no unusual anisotropy in the ADPs, thus this additional site likely originates from a structural feature and not twinning. This suggests the presence of disorder on the vanadium site, for example, a minor portion of the vanadyl ions having an orientation that is opposite to the majority. The addition of another vanadium atom at the position of the residual improved the refinement, and converged with an occupancy of 2%, suggesting that a small number of VO_6 octahedra have an inverted bonding pattern, and form local defects. The presence of the defects significantly deforms the V—O—S bond angles between neighboring chains, increasing from 136.6° to 137–149°.

3.1. Disorder in β-$VOSO_4$

The defects can either be distributed randomly or in a correlated fashion, and this information is encoded in the diffuse scattering data. As illustrated in Fig. 3, we observe rod-like diffuse scattering propagating along $\mathbf{b}^*$. The diffuse rods are centered at the Bragg nodes of the average structure with some intensity modulation along the rods. In particular, for the 3*kl* layer, the diffuse rods are present for all nodes except $l = 0$, whereas in the 4*kl* layer, the diffuse rods are only observed for the nodes with $k + l = 2n - 1$. Reconstructions of additional sections are available in the supporting information. Since the structure is centrosymmetric, we do not expect any violation of Friedel's law, therefore the apparent asymmetry in the intensity of the rods normal to $\mathbf{c}^*$ is due to limitations in the finite precision of the orientation matrix (given the extreme sharpness of the diffuse features), beam inhomogeneity and anisotropic crystal sizes.

The observed rod-like diffuse scattering corresponds to planar objects in real space, oriented normal to the crystallographic *b*-axis. This suggests that the defects are correlated such that they form thin layers in the *ac*-plane. Within the plane, the bonding pattern of the ordered structure is maintained, but layers of defects destroy the ideal alternating bonding pattern along the *b*-axis (Fig. 4), introducing disorder and leading to the diffuse maxima along $\mathbf{b}^*$. Correlations between these layers along the *b*-axis are also possible, and information about these can be extracted from the intensity modulations of the rods.

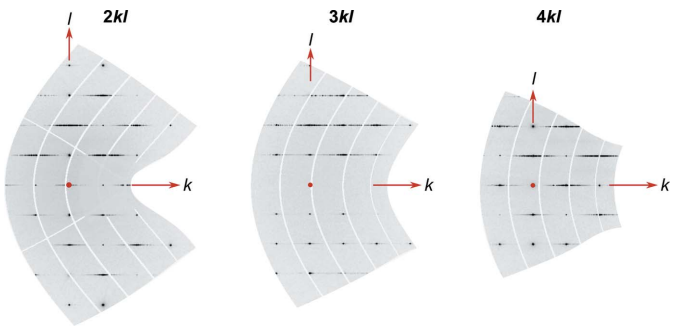

Figure 3
Reciprocal layers reconstructed from the ID28 data, showing the rod-like diffuse scattering measured with β-$VOSO_4$ crystals. The white gaps originate from the spacing between modules in the detectors.

Atomistic MC modeling is one method through which these correlations can be explored. Here, large disordered models with a defined correlation between layers are created and the calculated diffuse scattering patterns are qualitatively compared with the measured scattering patterns. The construction of models is illustrated in Fig. 4. The average unit cell from Bragg diffraction was expanded to a 40 × 100 × 40 supercell (296 × 630 × 285 $Å^3$), and 10% of the layers were randomly converted to defect layers by changing the orientation of the vanadyl bond (Fig. 4, left-hand view). The change was propagated throughout the *ac*-plane, making them perfectly periodic in accordance with the observed diffuse rods. To simplify the model further, each *ac*-plane can be represented as either 1 (for a normal layer) or −1 (for a defect layer), corresponding to the numbers underneath each layer in the supercell in Fig. 4. The configuration of the defects can then be visualized, as in Fig. 4 (right-hand view) as a chain along the *b*-axis with gray circles representing layers with the correct bonding pattern (1), and those in red representing defect layers (−1). Note that a larger percentage of defects (10% rather than 2%) was used in the modeling as we are limited to fairly small boxes (100 unit cells = 200 layers) so investigation of different ordering patterns would not be possible with such a low level of defects.

Correlations between defect layers were created using an MC algorithm. Layers were chosen at random and their vanadyl bonding orientation swapped. MC moves were then accepted based on the Ising-like energy function:

$$E = \sum_{i,j} -k_{ij}\sigma_i\sigma_j, \qquad (1)$$

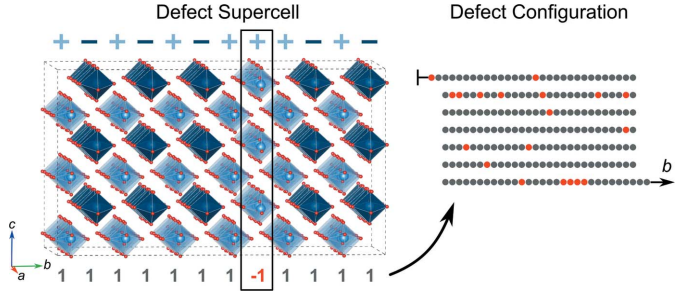

Figure 4
The creation of the models for diffuse scattering calculation. The average structure is expanded to a supercell (left, the SO_4 is left out for clearer visualization) where the light and dark polyhedra represent the + and − vanadyl bonding patterns, respectively. Planar defects are introduced into the structure by inverting the bonding pattern of all the VO_6 octahedra in the *ac*-plane, as shown by the black box. Each layer of octahedra (stacked along the *b*-axis) is assigned a pseudo-spin as indicated by the 1/−1 at the bottom, depending on their orientation relative to the ideal, therefore a complete *ac*-plane can be represented by one spin variable. The whole defect configuration can then be visualized as shown on the right, with gray and red circles representing regular and defect layers, respectively.

where σ = +/ − 1 are the pseudo-spin variables assigned to each layer to represent their orientation and k_{ij} is the interaction energy between spins i and j. The correlation along the b-axis is defined by the Warren–Cowley short-range order parameter

$$\alpha_v = 1 - \frac{P_v^{\sigma_i\sigma_j}}{m_i m_j}, \qquad (2)$$

where $P_v^{\sigma_i\sigma_j}$ is the probability of finding spins i and j next to each other along the inter-layer vector, v, and m_i and m_j are the average concentrations of each spin. To drive the system towards the desired correlation, the interaction energies were updated at the end of each MC cycle, to make moves more/less likely to be accepted depending on the difference between the target and current correlations.

The values of α_v vary between −1 and 1. Positive correlations correspond to the clustering of defect layers, which would correspond to the formation of domains of inverted bonding in the crystal. A correlation of zero indicates a random distribution of defects throughout the crystal, and negative correlations mean defects prefer not to be next to each other. Because there is not a 1:1 ratio between normal and defect layers in this model, multiple different configurations satisfy a negative correlation. Both configurations in Figs. 5(*c*) and (*d*) have a nearest neighbor correlation of −0.1, which is the most negative this concentration of defects can achieve. If every defect is isolated, $P^{\sigma_i\sigma_j}$ will be equal to the average defect concentration and thus, for the models used here, α = 1 − 0.1/(0.1*0.9) = −0.1111. Additionally, the configuration in Fig. 5(*c*) looks essentially the same as the random one above it, again reflecting the relatively low level of defects in the model. To distinguish between different configurations with negative correlations and move away from randomness towards defects being as far apart as possible, additional nearest neighbors need to be included in the model. For example, specifying a negative nearest neighbor correlation and a positive next-nearest neighbor correlation results in the alternating configuration in Fig. 5(*d*), and specifying ten layers of neighbors all with a negative correlation would lead to defects being evenly distributed as far apart as possible.

Several different correlation models were tested in order to produce various local defect structures. For each, 20 atomic configurations were generated, and reciprocal space sections of the diffuse scattering were calculated using the program *Scatty* (Paddison, 2019). The scattering from each of the configurations was averaged to improve the statistics and Lanczos resampling was employed to aid noise reduction. The Bragg scattering was subtracted from all reciprocal sections and the resulting diffuse scattering sections are shown in Fig. 5 along with examples of the defect configurations used to simulate them.

All the models reproduce the narrow diffuse rods in the correct places, indicating that the planar defects inferred from the diffuse scattering are reasonable models of the disorder in this material. It is also evident that the intensity modulations along **b*** are very sensitive to the inter-layer correlations, even the subtle difference between the models in Fig. 5(*c*) and 5(*d*).

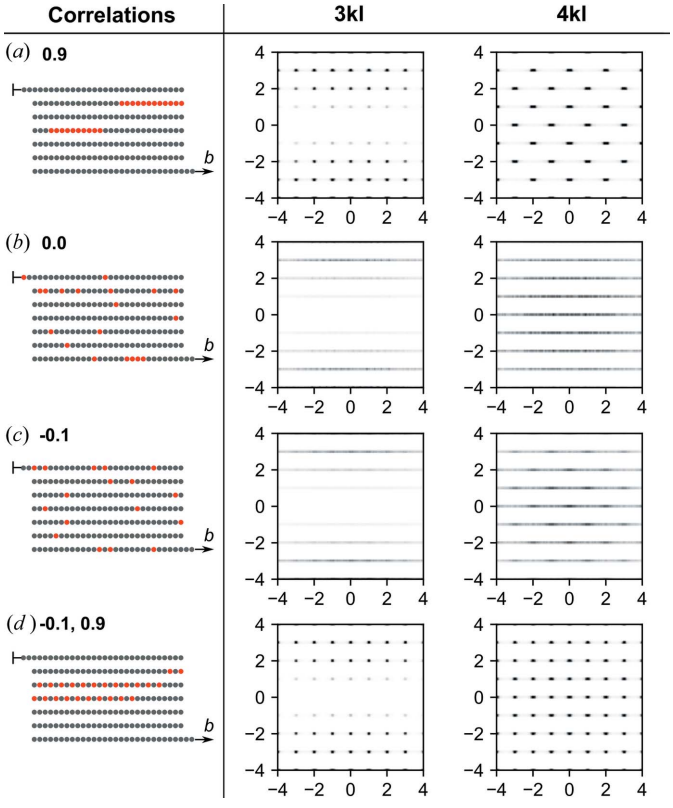

Figure 5
Views (*a*), (*b*), (*c*) and (*d*) show four different correlation models, where gray and red circles indicate normal and defect layers stacked along the b-axis, and the corresponding calculated diffuse scattering patterns for selected sections. For (*d*), the two correlation values correspond to that of the nearest neighbors and next-nearest neighbors.

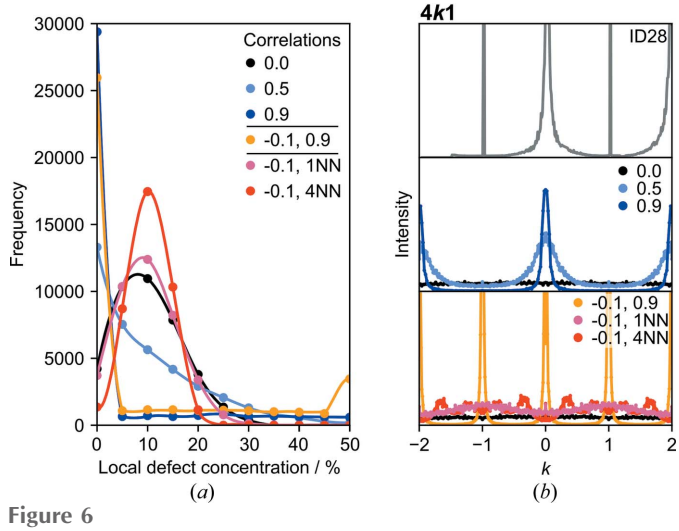

Figure 6
(*a*) Histograms of the local defect concentration for various correlation models, with the correlations quantified by α in equation (2). The labels −0.1 1NN and −0.1 4NN correspond to models with correlations of −0.1 spanning one and four nearest neighbors, respectively. (*b*) From top to bottom, the experimental scattering from ID28 and the calculated diffuse scattering patterns for positive and negative correlations along the 4*k1* direction.

The differences between each of these models can be more easily visualized in the plots in Fig. 6. Here, the left panel is a histogram of the local defect concentration in the model. A small section of the model (*e.g.* 20 layers) is examined and the defect concentration is calculated as a percentage. This is repeated, taking random sections each time, to build up the histogram which represents how the defects are distributed throughout the model. In the random model, we see a roughly Gaussian distribution of defects around the global average (10%). The corresponding calculated and experimental diffuse scattering for the 4*k*1 rod is then shown on the right for the different models. For the random model, the calculated intensity is featureless because there are no inter-layer correlations.

For positive inter-layer correlations, large portions of the model contain no defects, as they cluster together, therefore the peak in the histogram shifts towards lower concentrations. These models produce diffuse maxima at the correct Bragg nodes ($k + l = 2n - 1$ for 4*kl*) with respect to the experimental scattering, and they get narrower and more intense as the correlation becomes more positive, *i.e.* the antiphase domains in the crystal become larger. For negative correlations, an alternating configuration [as in Fig. 5(*d*)] produces two peaks in the histogram: one at 50% and one at 0%, showing that the model is made of sections where there is a strictly alternating pattern of defects and normal layers and sections which have no defects. The simulated diffuse scattering shows strong maxima at every Bragg node. As defects move from a random distribution to explicitly avoiding each other (achieved in the model by including more and more nearest neighbors with a negative correlation), the histogram peak remains centered on the global average but becomes narrower as the defects tend toward being evenly distributed in the model. The diffuse scattering is particularly sensitive to this and evolves non-trivially as we approach this limit.

A comparison of the experimental and simulated scattering suggests that a positive correlation gives the best description of the local defect structure in this material. Since the defects are in a higher concentration in the model and the correlations are not being refined, further analysis would need to be done before being able to extract quantitative parameters. In future work, improved model statistics could be achieved using a 3D approach, similar to Chan *et al.* (2010), and the correlation could be refined against the measured data, assuming the Bragg and diffuse scattering can be separated. Regardless, the positive correlation is enough to conclude that small domains of inverted bonding form in the crystal.

4. Discussion

Disorder in vanadyl bonds has previously been noted for several compounds, such as $Ba_2V_3O_9$ (Dhaussy *et al.*, 1996), $BiCu_2(P_{1-x}V_x)O_6$ (Mentré *et al.*, 2006), $Pb_2V_3O_9$, $Pb_2As_2VO_9$ (Mentré *et al.*, 1999), $(VO)_2P_2O_7$ (Hiroi *et al.*, 1999) and $Na_xV_2O_5$ (Krogstad *et al.*, 2020). However, none of these studies have been conclusive in this regard, due to the influence of very low-symmetry space groups, chemical impurities, crystal quality, and ion diffusion. Here we present clear indications of a new type of defect in high-quality β-$VOSO_4$ single crystals, namely 2D planar objects of the same vanadyl bonding pattern.

These defect layers could significantly affect the magnetic properties of the compound through multiple mechanisms. Firstly, the local magnetization of vanadium will be slightly deformed by the polarization effects of π-bonding in the vanadyl ions (Ballhausen & Gray, 1962). Secondly, the change of the bonding patterns in the neighboring chains connected via SO_4 might affect the intra-chain magnetic interaction, cutting the spin chain and creating free $S = \frac{1}{2}$ contributions. In theory, at high concentrations, these defects could induce a spin-Peierls instability (Seidel *et al.*, 2003) driving the compound to dimerization, but it is unclear what the defects convey at low concentrations. This is especially relevant at high magnetic fields near the field-induced long-range magnetic order, where spin-nematic and spin-glass phases have been proposed (Büttgen *et al.*, 2014). It is also likely that these defects have an influence on the lack of long-range magnetic ordering reported down to 0.1 K (Quintero-Castro *et al.*, 2022, in preparation). Furthermore, the lack of inversion symmetry at the boundaries between defect layers opens the possibility for Dzyaloshinskii–Moriya interactions (DMI) to arise, which would open a magnetic field-dependent spin gap modifying the system's magnetic phase diagram (Oshikawa & Affleck, 1997).

5. Conclusions

The crystal structure and disorder in β-$VOSO_4$ have been elucidated through single-crystal diffraction and atomistic modeling. The structure was found to contain defects, whereby 2% of the VO_6 octahedra have inverted vanadyl bonding patterns. Diffuse scattering analysis suggested that these defects are correlated, forming planes of defects normal to the crystallographic *b*-axis and disrupting the alternating bonding pattern. Atomistic modeling shows that further correlations between defect planes are present in β-$VOSO_4$ such that defect layers are clustered together forming small antiphase domains of inverted vanadyl bonding patterns. These defects are not mobile at ambient conditions and we expect them to be created during crystallization. The 2D defect layers represent a new type of defect in these systems, one which is likely to impact the magnetic properties and potentially facilitate unusual magnetic interactions. In this respect, the defect β-$VOSO_4$ structure offers a new and as yet unexplored playground for the study of the relationships between disorder and magnetic properties.

Acknowledgements

CAF, VD and DC thank colleagues from Swiss–Norwegian Beamlines for their friendly support. DC is also grateful to Professor Rodolphe Clerac for fruitful discussions on magnetic interactions.

References

Ballhausen, C. J. & Gray, H. B. (1962). *Inorg. Chem.* **1**, 111–122.

Büttgen, N., Nawa, K., Fujita, T., Hagiwara, M., Kuhns, P., Prokofiev, A., Reyes, A. P., Svistov, L. E., Yoshimura, K. & Takigawa, M. (2014). *Phys. Rev. B*, **90**, 134401.

Chan, E. J., Welberry, T. R., Heerdegen, A. P. & Goossens, D. J. (2010). *Acta Cryst.* B**66**, 696–707.

Chávez, N. C., Mattiotti, F., Méndez-Bermúdez, J. A., Borgonovi, F. & Celardo, G. L. (2021). *Phys. Rev. Lett.* **126**, 153201.

Dhaussy, A.-C., Abraham, F., Mentre, O. & Steinfink, H. (1996). *J. Solid State Chem.* **126**, 328–335.

Dyadkin, V., Pattison, P., Dmitriev, V. & Chernyshov, D. (2016). *J. Synchrotron Rad.* **23**, 825–829.

Fang, J.-K., Huang, J., Wu, H.-Q. & Yao, D.-X. (2021). *Front. Phys.* **17**, 33503.

Girard, A., Nguyen-Thanh, T., Souliou, S. M., Stekiel, M., Morgenroth, W., Paolasini, L., Minelli, A., Gambetti, D., Winkler, B. & Bosak, A. (2019). *J. Synchrotron Rad.* **26**, 272–279.

Haldane, F. (1983). *Phys. Lett. A*, **93**, 464–468.

Hiroi, Z., Azuma, M., Fujishiro, Y., Saito, T., Takano, M., Izumi, F., Kamiyama, T. & Ikeda, T. (1999). *J. Solid State Chem.* **146**, 369–379.

Krivovichev, S. V., Vergasova, L. P., Britvin, S. N., Filatov, S. K., Kahlenberg, V. & Ananiev, V. V. (2007). *Can. Mineral.* **45**, 921–927.

Krogstad, M., Rosenkranz, S., Wozniak, J., Jennings, G., Ruff, J., Vaughey, J. & Osborn, R. (2020). *Nat. Mater.* **19**, 63–68.

Laurell, P., Scheie, A., Mukherjee, C. J., Koza, M. M., Enderle, M., Tylczynski, Z., Okamoto, S., Coldea, R., Tennant, D. A. & Alvarez, G. (2021). *Phys. Rev. Lett.* **127**, 037201.

Longo, J. & Arnott, R. (1970). *J. Solid State Chem.* **1**, 394–398.

Marchukov, O., Volosniev, A., Valiente, M., Petrosyan, D. & Zinner, N. (2016). *Nat. Commun.* **7**, 13070.

Mathew, G., Silva, S. L. L., Jain, A., Mohan, A., Adroja, D. T., Sakai, V. G., Tomy, C. V., Banerjee, A., Goreti, R. N. A. V., Singh, R. & Jaiswal-Nagar, D. (2020). *Phys. Rev. Res.* **2**, 043329.

Mentré, O., Dhaussy, A. C., Abraham, F., Suard, E. & Steinfink, H. (1999). *Chem. Mater.* **11**, 2408–2416.

Mentré, O., Ketatni, E. M., Colmont, M., Huvé, M., Abraham, F. & Petricek, V. (2006). *J. Am. Chem. Soc.* **128**, 10857–10867.

O'Connor, C. J., Soghomonian, V., Haushalter, R. C., Wang, Z. & Zubieta, J. (1994). *J. Appl. Phys.* **75**, 5859–5861.

Oshikawa, M. & Affleck, I. (1997). *Phys. Rev. Lett.* **79**, 2883–2886.

Paddison, J. A. M. (2019). *Acta Cryst.* A**75**, 14–24.

Petrović, A., Ansermet, D., Chernyshov, D., Hoesch, M., Salloum, D., Gougeon, P., Potel, M., Boeri, L. & Panagopoulos, C. (2016). *Nat. Commun.* **7**, 12262.

Qin, S., Ng, T.-K. & Su, Z.-B. (1995). *Phys. Rev. B*, **52**, 12844–12848.

Rigaku Oxford Diffraction (2015). *CrysAlis Pro* Software system, Version 1.171.38.41. Rigaku Oxford Diffraction, Yarnton, England.

Seidel, A., Marianetti, C. A., Chou, F. C., Ceder, G. & Lee, P. A. (2003). *Phys. Rev. B*, **67**, 020405.

Sheldrick, G. M. (2008). *Acta Cryst.* A**64**, 112–122.

Sieverts, A. & Müller, E. L. (1928). *Z. Anorg. Allg. Chem.* **173**, 313–323.

Vasiliev, A., Volkova, O., Zvereva, E. & Markina, M. (2018). *npj Quantum Materials*, **3**, 18.

Villeneuve, G., Lezama, L. & Rojo, T. (1989). *Mol. Cryst. Liq. Cryst. Incorporating Nonlinear Opt.* **176**, 495–505.

Xiao, F., Blackmore, W. J. A., Huddart, B. M., Gomilšek, M., Hicken, T. J., Baines, C., Baker, P. J., Pratt, F. L., Blundell, S. J., Lu, H., Singleton, J., Gawryluk, D., Turnbull, M. M., Krämer, K. W., Goddard, P. A. & Lancaster, T. (2020). *Phys. Rev. B*, **102**, 174429.